Research Article

Chunyan Jia* and Mengyang Lu

Unequal width T-node stress concentration factor analysis of stiffened rectangular steel pipe concrete

https://doi.org/10.1515/nleng-2025-0174
received April 4, 2025; accepted August 19, 2025

Abstract: T-node tensile specimens, including both rectangular steel pipes and rectangular steel pipe concrete configurations, were developed based on the results of tensile tests conducted on concrete-filled rectangular steel pipe T-nodes. The specimens incorporated Perfobond Leiste (PBL) stiffeners, with concrete-filled rectangular steel pipes used for the main pipes and square steel pipes as the branch (stub) pipes. The fatigue performance of the concrete-filled rectangular steel pipe T-nodes under tensile loading, in-plane bending, and out-of-plane bending was investigated using PBL stiffeners as internal reinforcement. To determine the stress concentration parameters of the branch pipes, a nonlinear finite element analysis was performed using ABAQUS (a finite element analysis software suite developed by Dassault Systèmes) software. The analysis adopted a width-to-thickness ratio of 0.4 for the branch pipe and 27 for the main pipe. The results indicate that the hot spot locations of the PBL-stiffened concrete-filled rectangular steel pipe T-nodes are consistent with those of both the unstiffened rectangular steel pipe nodes and the concrete-filled nodes. Furthermore, the stress concentration factor of the PBL-stiffened node is significantly lower than that of the unstiffened steel pipe node, indicating markedly improved fatigue resistance.

Keywords: rectangular steel pipe concrete, T-node, PBL, stress concentration factor, nonlinear finite element analysis

*** Corresponding author: Chunyan Jia,** Civil Engineering and Transportation Engineering, Yellow River Conservancy Technical University, Kaifeng, Henan, 475004, China,
e-mail: jcy2009@163.com
Mengyang Lu: Civil Engineering and Transportation Engineering, Yellow River Conservancy Technical University, Kaifeng, Henan, 475004, China

1 Introduction

Open-cell steel plates, also known as Perfobond Leiste (PBL) stiffening ribs, are embedded longitudinally along the inner wall of steel pipes to form PBL-stiffened steel pipe concrete structures, which are subsequently filled with concrete [1,2]. These ribs serve dual functions: providing internal stiffening and acting as shear connectors. Their inclusion enhances the bond strength at the steel–concrete interface, reduces relative slip, and prevents interface spalling in the node area – thereby improving the tensile stiffness and load-carrying capacity of the node.

Previous studies have extensively investigated the stress concentration factors (SCFs) of T-welded rectangular steel pipe nodes [3], offering empirical formulas and identifying likely hot spot locations. It has been shown that filling steel pipes with concrete can significantly reduce SCFs – by 15–80% – and increase fatigue life by approximately 1.7 times compared to hollow steel pipe nodes [4]. Research also suggests that while the S–N curve of steel pipe nodes may still be applicable, hot spot stresses must be carefully managed [5]. Additional tests confirm the superior fatigue performance of steel pipe concrete nodes under axial and bending loads, with more uniform stress distributions than their hollow counterparts [6].

Building on this foundation, this study focuses on T-node stubs for rectangular steel pipe concrete, incorporating PBL stiffeners. Through tensile experiments, we compare stress characteristics among rectangular steel pipe nodes, concrete-filled nodes, and PBL-stiffened nodes. The results reveal that PBL stiffeners significantly reduce axial stress and enhance uniformity of stress distribution at the node root. This article further analyzes changes in hot spot locations and SCFs across different node configurations, and evaluates the fatigue resistance of the proposed PBL-stiffened structure. The findings aim to provide technical support for the application of such nodes in steel pipe concrete bridge engineering [7,8].

The main steel pipe's width/thickness ratio, the branch main pipe's width/thickness ratio, the concrete filling

inside the pipe, the positioning of the PBL stiffening ribs, and other factors are some of the many variables that affect the fatigue performance of steel pipe T-nodes [9]. In order to examine the impact of PBL stiffening ribs on the SCF of the uneven width T-node, this study develops the tensile test of PBL-stiffened rectangular steel pipe concrete node based on the tensile test of T-node designed by Packer. The literature is in agreement with the main pipe's constructional dimensions, material parameters, and branch pipe width. β = 0.4 is the width ratio of the branch pipe to the main pipe. The test reported in the literature states that the wall thickness of the branch pipe is adjusted to 6.32 mm, which is thicker than the wall thickness of the main pipe (4.74 mm), in order to prevent axial tension damage to the branch pipe [10]. This test is intended to analyze the node's bearing capacity. The branch pipe wall's thickness is decreased to 4.74 mm, which, in keeping with the test's goals as outlined in this document, is the same thickness as the main pipe wall. The yield strength of the main pipe and the branch pipe steel is f_y = 400 MPa, the ultimate tensile strength is f_u = 544 MPa, and the compressive strength of the concrete cylinder is f_c = 30.0 MPa. Figure 1 displays the specimen structure, while Table 1 displays the precise design parameters.

Table 1 summarizes the geometric parameters and data sources of different specimens, including T1 and T1C from the referenced literature and T1PLB from this article. All three specimens share identical main geometric dimensions: main steel pipe outer diameter of 125.6 mm, side length of 174.5 mm, wall thickness of 4.12 mm; branch pipe outer diameter of 50.1 mm, side length of 52.2 mm, wall thickness of 4.21 mm; with a width-to-thickness ratio of 0.32; and a PBL stiffening rib spacing of 25 mm. This indicates that the T1PLB specimen in this study maintains consistent geometry with previous research but mainly differs in structural details such as the addition of PBL stiffeners for comparative analysis [11].

2 Numerical simulation

The branch pipe's connection welds and the contact nonlinearity at the steel–concrete interface are taken into consideration in this work because they have a substantial impact on the node's stress concentration coefficient. Since the branch pipe of the T-node encounters moderate amounts of stress under tensile, in-plane, and out-of-plane bending when both are in an elastic operating condition, material and geometrical nonlinearities do not need to be taken into consideration in the model.

The loading patterns of specimens T1, T1C, and T1PBL are displayed in Figure 2. Figure 2(a) applies an axial tensile load P of 1 MPa to the specimens T1, T1C, and T1PBL; Figure 2(b) shows that the specimens T1, T1C, and T1PBL experience an in-plane bending moment Min, which results in a tensile stress of 1 MPa in the steel pipe outside the stub's root; and Figure 2(c) shows that the specimens T1, T1C, and T1PBL experience an out-of-plane bending moment that acts on them and produces a tensile stress of 1 MPa in the steel pipe outside the root of the mouth movement.

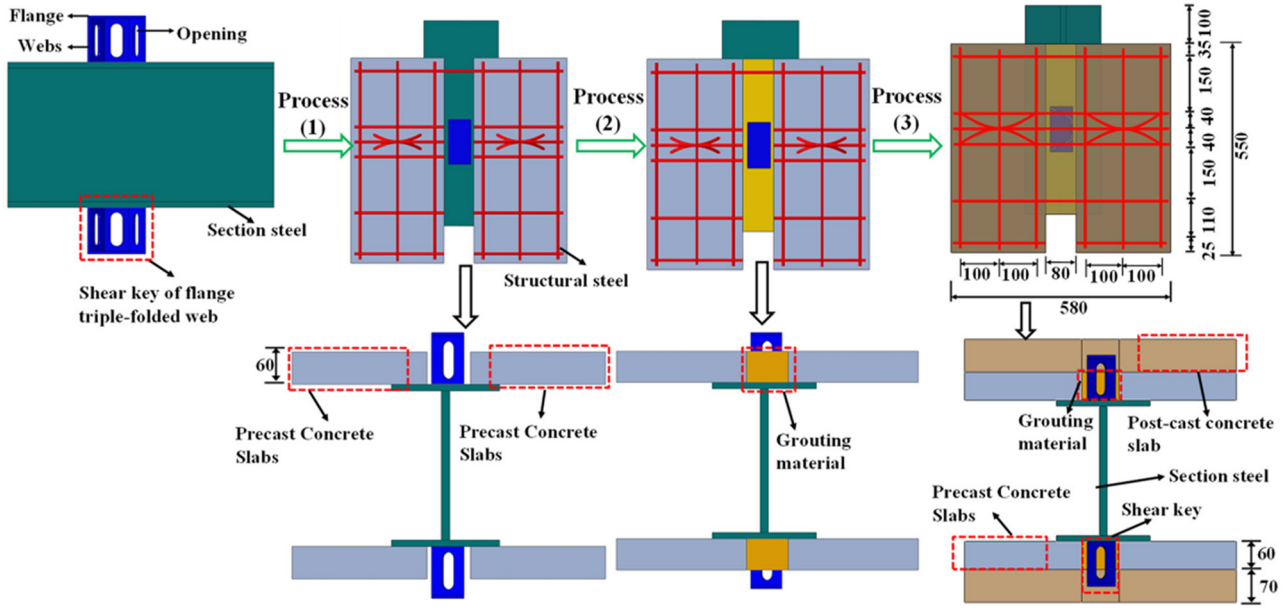

Figure 1: Test piece construction form.

Table 1: Specimen parameters

Data sources	Test piece number	b_0 (mm)	h_0 (mm)	t_0 (mm)	b_1 (mm)	h_1 (mm)	t_1 (mm)	β (mm)	γ (mm)
Ref. [10]	T1	125.6	174.5	4.12	50.1	52.2	4.21	0.32	25
	T1C	125.6	174.5	4.12	50.1	52.2	4.21	0.32	25
This article	T1PLB	125.6	174.5	4.12	50.1	52.2	4.21	0.32	25

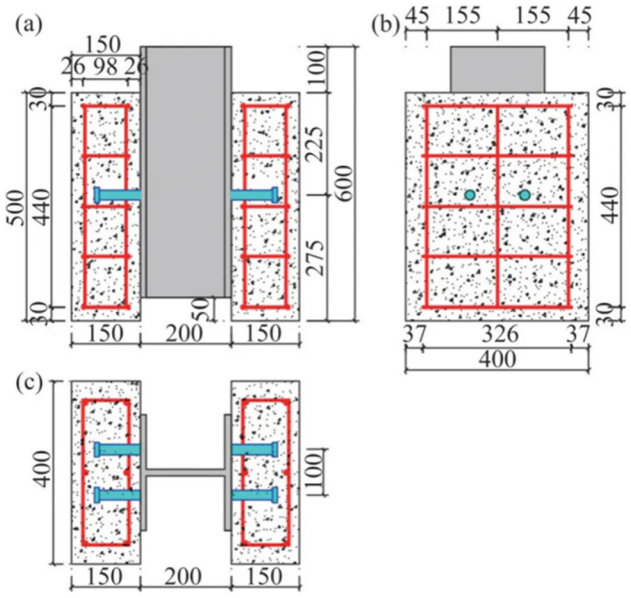

Figure 2: Specimen loading mode.

2.1 Steel and concrete structures' relationship

In steel–concrete composite structures, the interaction between steel and concrete components plays a crucial role in determining the overall mechanical behavior and load-bearing capacity. Both steel and concrete materials are typically modeled using the linear elastic stress–strain relationship under service load conditions, which assumes a proportional and reversible response between stress and strain within the elastic limit.

For steel, this linear elastic behavior is characterized by a relatively high modulus of elasticity and a well-defined yield point, allowing for accurate prediction of deformation under applied loads. Concrete, although more brittle and heterogeneous than steel, is often idealized as a linear elastic material before cracking occurs. The linear elastic assumption simplifies the analysis of initial stiffness and stress distribution in composite members.

The compatibility of deformation between steel and concrete is ensured through effective bonding or mechanical connectors, which transfer stresses across the interface. This interaction allows the composite structure to benefit from the high tensile strength and ductility of steel, combined with the compressive strength and stiffness of concrete.

However, it is important to note that beyond the elastic range, concrete exhibits nonlinear behavior due to cracking and crushing, while steel shows plastic deformation. Thus, for ultimate strength or failure analyses, more advanced constitutive models are required to capture the inelastic behavior of both materials and their interaction mechanisms.

In summary, the linear elastic stress–strain relationship provides a fundamental and practical basis for modeling steel and concrete components in composite structures during the initial loading stages, facilitating structural design and preliminary performance evaluation.

2.2 Modeling of the steel–concrete interface contact

The master surface at the steel–concrete interface is represented by the normal contact and tangential bond–slip contact models, which is the concrete, and the slave surfaces, which are the steel pipe and PBL stiffening ribs, which have more stiffness. In the normal contact between the steel box and concrete interface, which adheres to the "hard" contact paradigm, the contact surface transmits the interfacial pressure p. According to the Coulomb friction model, the tangential contact occurs when the interfacial shear stress $\tau \le \tau_e$, the interface does not move relative to one another; conversely, when $\tau \le \tau_e$, the interface moves relative to one another and the shear stress remains at τ_e, where τ_e denotes the critical value of the shear force, the average bond strength of the interface, $\tau_u = 0.462$ MPa, and the critical value, $\tau_e = u_p > \tau_u$ [12,13]. The interfacial friction factor (μ) in this case is defined as $\mu = 0.3$. In Figure 3, the contact model is displayed. The interfacial bond–slip shear modulus, κ, is represented by s, the total slip, and is assumed to be 0.165 MPa.

2.3 Selection of cell types and model meshing

The ABAQUS simulation model employs different element types for various components: the steel pipe and PBL stiffening ribs are modeled using S4R four-node reduced integration shell elements and C3D8R eight-node reduced integration hexahedral elements, respectively. The concrete filled inside the rectangular steel pipe is also modeled using these element types. However, due to the complexity of meshing hexahedral elements and the relatively minor impact of stress accuracy in the concrete region – attributed to the presence of PBL mortise and tenon connectors within the PBL-stiffened rectangular steel pipe – this study adopts C3D4 four-node tetrahedral elements for the concrete simulation. The end plates are represented by rigid surfaces. Figure 4 illustrates the meshing of the concrete T-node in the PBL-stiffened rectangular steel pipe. To minimize mesh transition issues, a sweep meshing technique is applied throughout the model.

2.4 Welded seam simulation

Using a S8R6 thick shell unit, the fillet weld on the branch main connection is simulated. The simulation of the weld shell unit is depicted in Figure 5, where t_w is the weld unit's effective thickness and l_f is the weld unit's predicted length

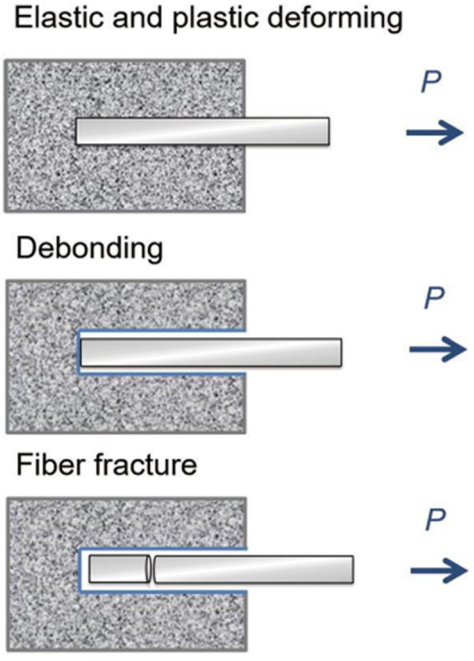

Figure 3: Contact model.

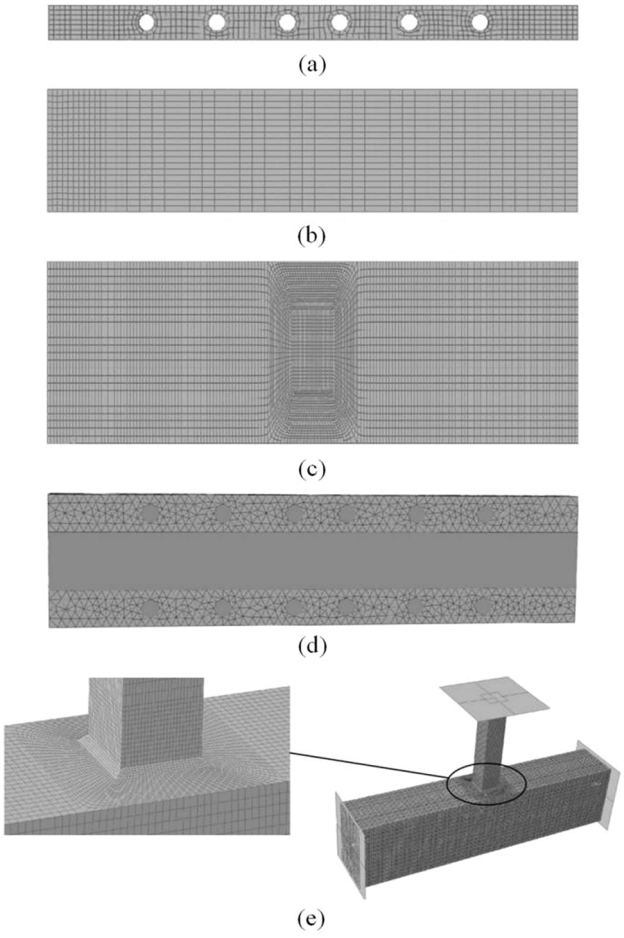

Figure 4: Grid division: (a) PBL stiffener, (b) branch pipe steel pipe, (c) main steel pipe, (d) concrete in the pipe, and (e) junction model.

($t_w = 0.5a_v a_h$). $\sqrt{a_v^2 + a_h^2}$, $l_f = \sqrt{(a_v + 0.5t_1)^2 + (a_h + 0.5t_0)^2}$. The thickness of the main pipe wall (t_0) is determined by measuring the horizontal length of the actual weld corner, a_v, and the thickness of the branch pipe wall (t_1) is determined by measuring the vertical length of the actual weld corner, a_h [14]. The bold black line in Figure 5 represents the midplane of the pipe wall of the main pipe and branch pipe, and the black region represents the fillet weld. The simulated shell unit of the main pipe, branch pipe, and weld is represented by the black region.

2.5 Boundary conditions

The end plate, branch pipe, and main pipe are all bounded. Its center is where the reference points RP-1, RP-2, and RP-3 are located, and they are connected to it. The x, y, and z directions of translational freedom as well as the x and z directions of rotational freedom delimited the RP-1 and

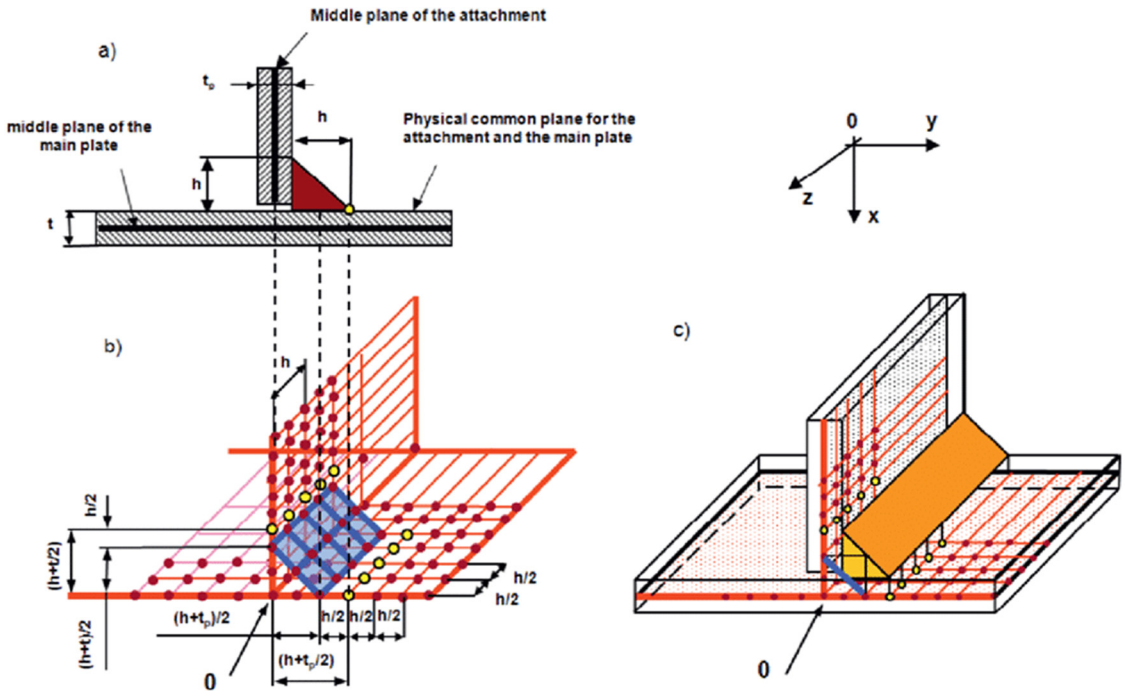

Figure 5: Simulation of the welded shell unit.

RP-2 reference points. The centralized load F is applied to reference point RP-3 in accordance with the force requirements. The following formulas can be used to calculate the equivalent centralized loads for the branch pipe's axial tensile, in-face bending, and out-of-face bending: F_{axial}, F_{imb}, and F_{omb}:

$$F_{\text{axial}} = 4b_1t_1, \tag{1}$$

$$F_{\text{imb}} = \frac{b_1^4 - (b_1 - 2t_1)^4}{6b_1L_1}, \tag{2}$$

$$F_{\text{omb}} = \frac{h_1^4 - (h_1 - 2t_1)^4}{6h_1L_1}, \tag{3}$$

where b_1 is the in-plane bending equivalent concentrated force (N), L is the target in-plane bending moment (N·m), h_1 is the branch pipe outer diameter or characteristic height (m), and t_1 is the branch width or characteristic length (m).

3 Results

3.1 Estimating where hot spots are most likely to be

Finding the hot spot's location is the first step in applying the hot spot stress method to analyze T-nodes' fatigue performance. The German specification CIDECT 8 provides the potential locations of hot spots in rectangular steel pipe nodes along with the appropriate stress concentration parameters [15]. The location of the hot spot is thought to be consistent with that of the rectangular steel pipe node, when the stress concentration coefficient of the rectangular steel pipe concrete T-node with bending in the branch pipe's face and axial force in the branch pipe is studied, as shown by the line ABCD in Figure 6. The location of the hot spot of the rectangular steel pipe concrete node of the PBL stiffener can be ascertained through examining the stress distribution law perpendicular to the direction of the weld seam; in other words, the maximum stress perpendicular to the weld direction is considered to be the hot spot stress rather than the maximum primary stress [16].

The stress contour distributions are illustrated in Figure 6. When the branch pipe is subjected to tension, the stress distribution in the T-node, evaluated perpendicular to the weld direction, reveals notable differences. By comparing specimens T1 and T2, it is observed that under axial loading on the branch pipe, the stress level on the branch pipe wall plate parallel to the main pipe's axial direction is higher than that on the wall plate perpendicular to it in specimens T1C and T1PBL. For the main pipe, the highest stresses occur along line segments B or C, whereas for the branch pipe, the maximum stresses are concentrated at line segments A or E.

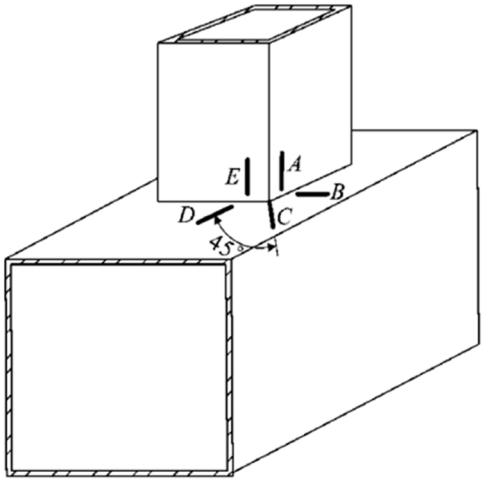

Figure 6: Location of hot spots.

During in-plane bending of the branch pipe, comparison of specimens T1, T1C, and T1PBL shows that the branch pipe's maximum stresses consistently appear at line segments A or E, while the main pipe's maximum stresses occur at line segments C or D.

Under out-of-plane bending of the branch pipe, the stress distribution comparison also indicates that the main pipe's peak stresses are located at line segments B or C, with the branch pipe's maximum stresses at line segments A or E.

These observations demonstrate that, in PBL-stiffened rectangular steel pipe nodes, the locations of stress hot spots align closely with those found in both rectangular steel pipe nodes and concrete-filled rectangular steel pipe nodes, confirming a consistent pattern of stress concentration across these node types.

3.2 SCF comparison

The branch pipe in this study has a nominal stress of 1 MPa, and the SCF is the hot spot stress. The hot spot stress of the main and branch pipes divided by their nominal stress is known as the SCF. The rectangular steel pipe and rectangular steel pipe concrete's hot spot stress concentration coefficient, and PBL reinforced rectangular steel pipe concrete node is determined by using the quadratic extrapolation method [17].

Figure 7 illustrates the SCFs at line segments A, B, C, D, and E for each specimen under axial tension of the stub.

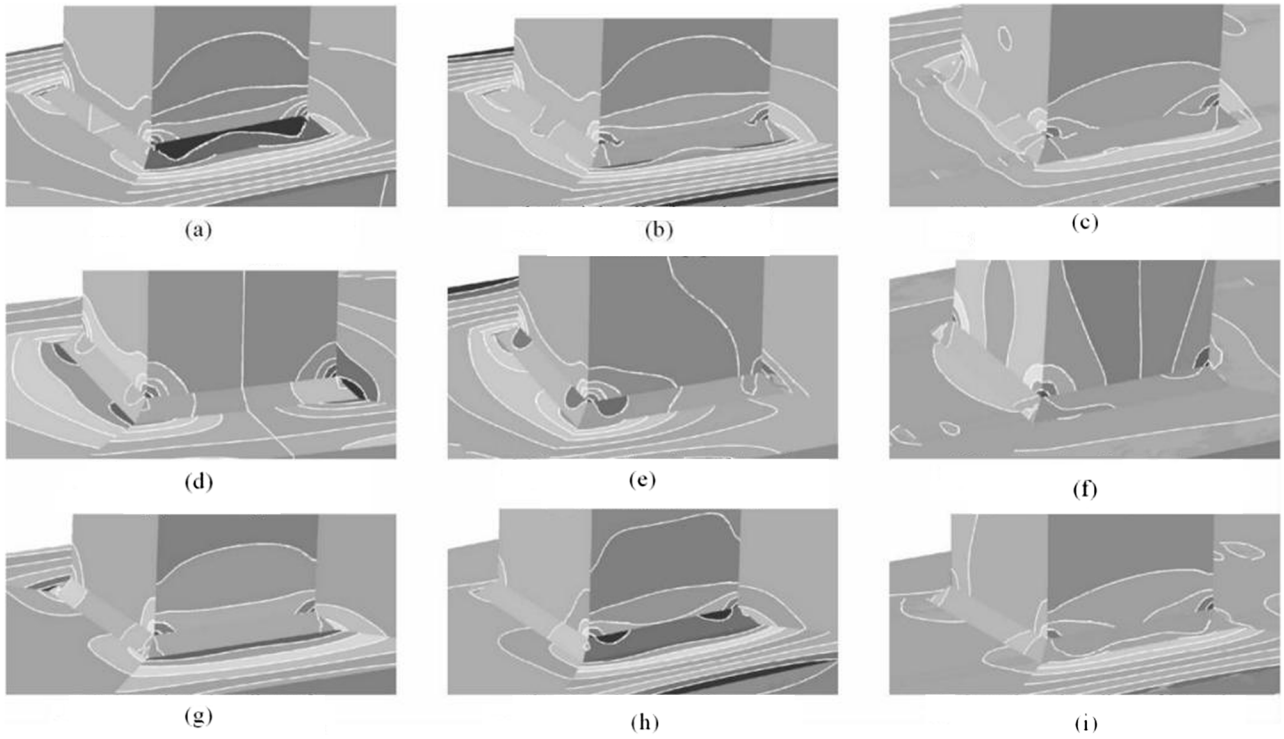

Figure 7: Stress contours: (a) axial pull of specimen T1 branch pipe, (b) axial pull of specimen T1C branch pipe, (c) axial pull of specimen T1PBL branch pipe, (d) in-plane bending of branch pipe T1 of specimen, (e) in-plane bending of branch pipe T1C of specimen, (f) in-plane bending of branch pipe T1PBL of specimen, (g) out-plane bending of branch pipe T1 of specimen, (h) out-plane bending of branch pipe T1C of specimen, and (i) out-plane bending of branch pipe T1PBL of specimen.

The SCF of specimen T1-CIDECT 8 is calculated according to the German CIDECT 8 specification [18].

Figure 8 presents a comparative analysis of SCFs at various hotspot locations for different pipe configurations during axial loading. Four configurations are included: T1-CIDECT, T1, T1C, and T1PBL. The SCF values for each configuration at different hotspots are summarized as follows:

Location A: At hotspot A, the SCFs of T1 and T1-CIDECT are relatively high, whereas those of T1C and T1PBL are lower. This indicates that T1 and T1-CIDECT configurations are more prone to stress concentration at this location.

Location E: Only T1-CIDECT exhibits a significant increase in SCF at position E, while the other configurations show comparatively lower values. This suggests that T1-CIDECT experiences greater stress concentration at this point, whereas the other configurations are less affected.

Location B: Position B has the highest SCF among all hotspots. The SCFs for T1 and T1C are significantly higher than those for T1-CIDECT and T1PBL, indicating that this location is especially susceptible to stress concentration in the T1 and T1C configurations and may represent a structural weak point.

Location C: The SCFs at position C are the second highest after position B. At this location, T1 and T1PBL exhibit relatively higher SCFs, while T1-CIDECT and T1C show somewhat lower values. This suggests that T1 and T1PBL configurations may also experience notable stress concentrations here.

Location D: At position D, all configurations display relatively low SCFs, though T1PBL shows a slightly higher value compared to the others. This indicates that the T1PBL configuration may be subjected to slightly greater stress at this location.

The calculated values of the SCF of the main pipe at line segments B, C, and D are close to the numerical simulation results in this article. It demonstrates the accuracy of the numerical simulation approach used in this work. The computed values of the branch pipe's SCF at line segments A and E, as shown in Figure 8, are quite similar to the average value computed in this work. The SCF of the rectangular steel pipe concrete node is smaller than that of the rectangular steel pipe node, which is consistent with the findings in the literature [6]. The SCF of the PBL-stiffened rectangular steel pipe concrete node is significantly smaller than that of the rectangular steel pipe concrete node. These results come from comparing the SCFs of specimens T1, T1C, and T1PBL at the hot spot locations. The maximum SCFs for branch pipes of rectangular steel pipe, rectangle steel pipe concrete, and PBL enhanced rectangular steel pipe concrete nodes all appeared at line segment A, but the maximum SCFs for main pipes all showed at line segment B.

Figure 9 shows a comparative analysis of the SCF at different hot spots during pipe bending for three different configurations: T1, T1C, and T1PBL. The stress concentration at different hot spots for each configuration is shown below:

Position A: At position A, the T1 configuration has the highest SCF, followed by T1C and T1PBL. This indicates that at position A, the T1 configuration is most prone to stress concentration, while the T1PBL configuration has less stress concentration [19].

Position E: At this position, the T1C configuration has a higher SCF than the other two configurations, the T1 has a slightly lower SCF, and the T1PBL has the lowest SCF. This indicates that the T1C configuration has the most significant stress concentration at Position E.

Position B: The SCF values for Position B are relatively high, and the SCFs of the T1 and T1PBL configurations are close to each other, while the SCF of T1C is relatively low, indicating that the T1 and T1PBL configurations have a high degree of stress concentration at this position.

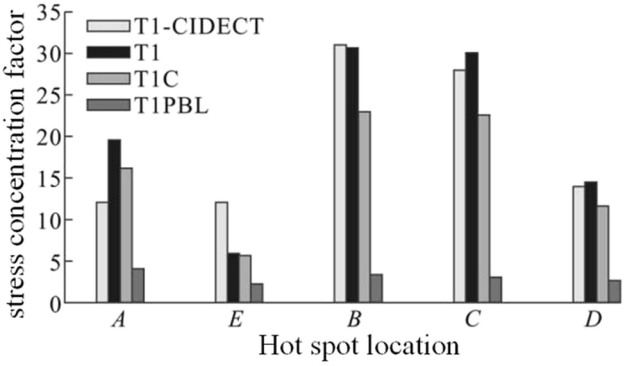

Figure 8: Comparative analysis of SCF in pipe shaft pulling with branches.

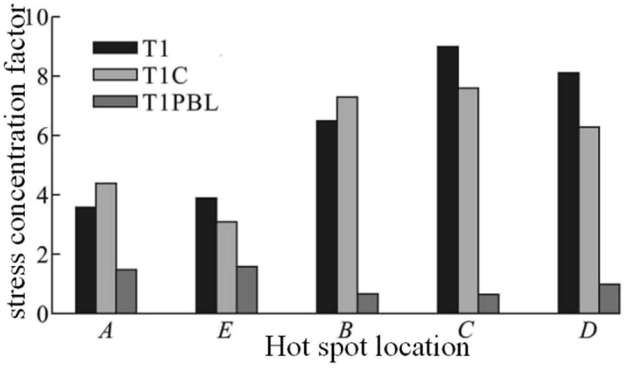

Figure 9: Comparison of stress concentration variables for branch pipe bending in the face.

Position C: At position C, the SCF of the T1 configuration is significantly higher than the other configurations, reaching the highest value in the figure, while the SCF of T1C and T1PBL are relatively low. This indicates that at position C, the T1 configuration has the most pronounced stress concentration and is a potential weak point [20–22].

Position D: The SCF value of position D is relatively low, the SCF value of T1C is slightly higher, and the SCF values of T1 and T1PBL are closer, indicating that the stress concentration of each configuration at this position is relatively small.

In summary, Figure 9 shows that there is a significant difference in the distribution of stress concentration at each hot spot in different configurations during pipe bending. In particular, the T1 configuration has the most significant stress concentration at position C and position B, while the T1PBL and T1C configurations have smaller stress concentrations at most positions. These data are helpful in selecting a reasonable configuration to reduce the stress concentration at a particular location.

When the branch pipe is bent out of face, Figure 10 shows the SCFs of each specimen at line segments A, B, C, D, and E. Figure 10 shows that the rectangular steel pipe concrete node's SCF is lower than the rectangular steel pipe node's; additionally, the PBL-stiffened rectangular steel pipe concrete node's SCF is significantly lower than the rectangular steel pipe node's. Line segment B displayed the maximum SCF for the rectangular steel pipe main pipe, rectangular steel pipe concrete, and PBL-stiffened rectangle steel pipe concrete nodes. Line segment E displayed the maximum SCF for the branch pipe.

In conclusion, when the branch pipe is subjected to axial tension – as opposed to in-plane or out-of-plane bending – the SCFs for rectangular steel pipe nodes, concrete-filled rectangular steel pipe nodes, and PBL-stiffened concrete-filled rectangular steel pipe nodes are all significantly increased. However, compared to hollow rectangular steel pipe nodes, the SCF of concrete-filled nodes is notably reduced, indicating that concrete infill helps to alleviate local stress concentration. Furthermore, the incorporation of PBL stiffening ribs in concrete-filled rectangular steel pipe nodes leads to a substantial improvement in fatigue resistance and a further reduction in SCF, thereby enhancing the overall structural performance of the node.

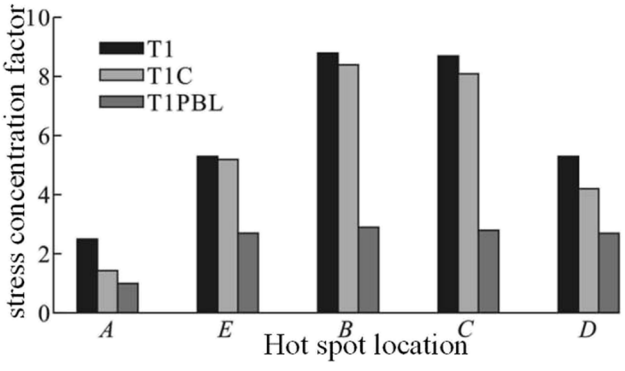

Figure 10: Compares the stress concentration parameters when bending a branch pipe outside of its face.

Although these findings are primarily based on nonlinear finite element simulations, they demonstrate clear mechanical advantages of the proposed node configuration. To enhance the credibility and engineering applicability of the results, subsequent physical experiments and validation tests are planned. These future efforts will provide empirical evidence to support the numerical findings, verify the fatigue behavior under real-world loading conditions, and further promote the use of PBL-stiffened rectangular steel pipe concrete nodes in structural applications such as bridge engineering and high-performance composite joints.

4 Conclusion

In summary, when the branch pipe is subjected to axial tension, the stress concentration coefficients of the rectangular steel pipe, steel pipe concrete node, and PBL-stiffened steel pipe concrete node increase significantly compared with the in-plane moment and out-of-plane moment conditions. Compared with the hollow rectangular steel pipe node, the filling of concrete can effectively reduce the degree of stress concentration; the further introduction of PBL stiffened ribs is more significant in improving the fatigue performance of the node, effectively reducing the stress concentration coefficient, and improving the overall load carrying capacity and fatigue life of the node.

This study is mainly based on nonlinear finite element simulation analysis, which has shown the advantages of PBL stiffened rectangular steel pipe concrete nodes in mechanical properties. In order to verify the reliability of the numerical simulation and improve the engineering applicability, solid tests or validation experiments will be carried out to obtain more convincing empirical data to further promote the application of this node form in practical engineering.

In addition, considering the excellent fatigue performance and structural adaptability of this node form, it is recommended to promote the application of this node form in steel–tube–concrete bridge structures, especially for

complex stress members or fatigue-sensitive parts, such as shaped nodes, diagonal nodes, cantilever connection zones, and transition nodes between the bridge deck system and the main structure. Future research can further explore the adaptability and construction optimization strategy of this node form under different structural forms and loading conditions, so as to enhance its application potential and promotion value in bridges and other large-span structural systems.

Funding information: Authors state no funding involved.

Author contributions: Chunyan Jia and Mengyang Lu designed the research together. Chunyan Jia conducted the main experiments, collected and analyzed the data, and drafted the initial manuscript. Mengyang Lu assisted in data validation, participated in result interpretation, and revised the manuscript critically for important intellectual content. Both authors read and approved the final version of the manuscript. All authors have accepted responsibility for the entire content of this manuscript and approved its submission.

Conflict of interest: Authors state no conflict of interest.

Data availability statement: The datasets generated during and/or analyzed during the current study are available from the corresponding author on reasonable request.

References

[1] Lu T, Li J, Xiao E, Zhong H, Deng J, Ma L, et al. Assemblage of root-associated microbiome contributes to disparate performance of two rice genotypes under aluminum stress. Plant Physiol Biochem. 2025;220:109539.

[2] Squitti R, Pal A, De Luca A, Rizzo G, Rongioletti M, Tondolo V. Exchangeable copper excess and zinc deficiency in the serum of patients with colorectal cancer. Biol Trace Elem Res. 2025;203(7):3548–58.

[3] Chunsheng W, Chuanzhong M, Jialei C, Hao QU, Wenchang W, Qinfeng DI. Analysis of secondary makeup characteristics of drill collar joint and prediction of downhole equivalent impact torque of well SDTK1. Pet Explor Dev. 2024;51(3):697–705.

[4] Diao Y, He S, Wang Y, Tu L. Experimental and numerical investigations on stress concentration factors of concrete filled steel tube X-joints. Sci Rep. 2024;14(1):11415.

[5] Ahmadian V, Aval SBB, Noori M, Wang T, Altabey WA. Comparative study of a newly proposed machine learning classification to detect damage occurrence in structures. Eng Appl Artif Intell. 2024;127:107226.

[6] Takeshita M, Tanaka A, Yoshida H, Nakamura I, Shibata Y, Hata S, et al. Effect of the xanthine oxidase inhibitor, febuxostat, on WBC count in asymptomatic hyperuricemia: subanalysis of the randomized PRIZE study. J Atheroscler Thrombosis. 2024;31(6):864–75.

[7] Zhang C, Roh B, Shan G. Poster: Dynamic clustered federated framework for multi-domain network anomaly detection. In Companion of the 19th International Conference on emerging Networking Experiments and Technologies; 2023. p. 71–2.

[8] Karam MS, Nakamura H, Yamamoto Y, Tahir M, Hameed R. Numerical evaluation of the internal fracture mechanism of the single PBL shear connector considering the effects of position and strength of the transverse rebar. Struct Concr. 2024;25(4):2759–83.

[9] Xue C, Huang H, Jia Q. Shear mechanism of a novel SFCBs-reinforced composite shear connector: experimental, theoretical investigations and numerical model. Materials. 2024;17(14):3508.

[10] Yang S, Hong Y, Pu Q, Ling X, Chen X, Wu K. Mechanical behaviour of steel–concrete joints in railway rigid frame-continuous composite system bridge. J Constr Steel Res. 2024;222:108946.

[11] Luo C, Wang X, Xu YJ, Jia S, Liu Z, Mao B, et al. Synergistic identification of hydrogeological parameters and pollution source information for groundwater point and areal source contamination based on machine learning surrogate-artificial hummingbird algorithm. EGUsphere. 2025;2025:1–54.

[12] Noda M, Kikuchi C, Hori E, Iwao T, Nagami C, Takeuchi M, et al. Effect of anagliptin on vascular injury in the femoral artery of type 2 diabetic rats. Biol Pharm Bull. 2024;47(1):204–12.

[13] Wang B, Wang C, Yin S, Du J, Yang X. Performance degradation of corrugated steel webs and concrete flange T-PBL connectors under fatigue loading. Int J Civ Eng. 2025;23(3):403–17.

[14] Du Y, Yu Z, Chen Y, Ma N, Wang R. Experimental study on the force mechanism of internal composite connectors in steel–concrete composite sections of bridge towers. Buildings. 2025;15(13):2284.

[15] Kumar P, Kota SR. Machine learning models in structural engineering research and a secured framework for structural health monitoring. Multimed Tools Appl. 2024;83(3):7721–59.

[16] Li A, Fan L, Tian X. Self-cruising environmental ship based on improved ant colony algorithm. In 2024 8th CAA International Conference on Vehicular Control and Intelligence (CVCI). IEEE; 2024. p. 1–6.

[17] Kumar SP, Beenamol M. Multiple layer radial basis neural network with remora regression tree optimum feature extraction for structural health monitoring. Asian J Civ Eng. 2023;24(4):989–99.

[18] Liu D, Miao C, Deng W, Zhang J, Zhang L, Gu J. Shear lag effect of steel–concrete composite girder bridge with steel truss webs: experiment, finite element, and theory. J Struct Eng. 2025;151(10):04025154.

[19] Yan B, Li C, Qiu M, Zhu Y, Hu M. Flexural performance of transverse wet joint in steel-UHPC composite beam under negative bending moments. J Constr Steel Res. 2024;223:109029.

[20] Wang Q, Li M, Chen C, Xu L, Fu Y, Xu J, et al. Glucose homeostasis controls N-acetyltransferase 10-mediated ac4C modification of HK2 to drive gastric tumorigenesis. Theranostics. 2025;15(6):2428.

[21] Vinayagam G, Thaiyan Rajendran R, Mohan MS, Stanislaus Arputharaj B, Jayakumar SS, Baskar S, et al. Multi-perspective investigations of aerosol's non-linear impact on unmanned aerial vehicle for air pollution control applications under various aerosol working environments. Aerosol Sci Eng. 2024;8(2):213–40.

[22] Wang W. Esg performance on the financing cost of A-share listed companies and an empirical study. Int J Hous Sci Appl. 2024;45(2):1–7.